nature portfolio

https://doi.org/10.1038/s41563-022-01266-6

Supplementary information

Enabling ultra-low-voltage switching in $BaTiO_3$

In the format provided by the authors and unedited

Supplementary Information

Enabling ultralow voltage switching in $BaTiO_3$

Y. Jiang[1,2], E. Parsonnet[3], A. Qualls[3], W. Zhao[1], S. Susarla[4], D. Pesquera[1,5], A. Dasgupta[1], M. Acharya[1,2], H. Zhang[1], T. Gosavi[6], C.-C. Lin[6], D. E. Nikonov[6], H. Li[6], I. A. Young[6], R. Ramesh[1,2,3], and L. W. Martin[1,2,*]

[1] Department of Materials Science and Engineering, University of California, Berkeley, Berkeley, CA 94720, USA

[2] Materials Sciences Division, Lawrence Berkeley National Laboratory, Berkeley, CA 94720, USA

[3] Department of Physics, University of California, Berkeley, Berkeley, CA 94720, USA

[4] National Center for Electron Microscopy, Molecular Foundry, Lawrence Berkeley National Laboratory, Berkeley, CA 94720, USA

[5] Catalan Institute of Nanoscience and Nanotechnology (ICN2), CSIC and BIST, Campus UAB, Bellaterra, 08193 Barcelona, Spain

[6] Components Research, Intel Corporation, Hillsboro, OR 97124, USA

* lwmartin@berkeley.edu

Table of Contents

Supplementary Notes

I. Literature Review on Electrical and Structural Properties of Ferroelectric Thin Films

An extensive literature review was made for $BaTiO_3$ films synthesized in the past 50 years with various techniques, including sputtering[1-8], molecular-beam epitaxy[9-13], pulsed-laser deposition[13-40], activated reactive evaporation[41-43], sol-gel process[44], hydrothermal reaction[45] and polymer precursor method[46]. The following describes the different summary figures as noted and how they were produced:

Figure 1a. This plot shows a summary of remanent polarization *vs.* coercive voltage. For any polarization-electric field (voltage) loop reported in previous studies, the coercive field (voltage), E_C (V_C) was extracted via taking average of the absolute values of positive E_C^+ (V_C^+) and negative E_C^- (V_C^-) [*i.e.*, $E_C = (|E_C^+|+|E_C^-|)/2$, $V_C = (|V_C^+|+|V_C^-|)/2$)] while the remanent polarization was extracted via taking average of the absolute values of positive P_r^+ and negative P_r^- [*i.e.*, $P_r = (|P_r^+|+|P_r^-|)/2$] after the correction of the loop for any horizontal bias, $(E_C^++E_C^-)/2$ or $(V_C^++V_C^-)/2$. The ferroelectric properties of a $BaTiO_3$ single crystal[13] are also shown.

Figure 1c. This plot shows a summary plot of the out-of-plane lattice expansion *vs.* coercive field. The out-of-plane lattice expansion was calculated using $\Delta l/l \times 100\%$ where l is the theoretical out-of-plane lattice parameter, $l_{theoretical}$ (*i.e.*, $l = l_{theoretical}$), while Δl is the difference between the measured out-of-plane lattice parameter, $l_{measured}$, and the theoretical out-of-plane lattice parameter (*i.e.*, $\Delta l = l_{measured} - l_{theoretical}$). For an epitaxially strained $BaTiO_3$ film on any substrate, $l_{measured}$ is directly obtained from θ-2θ X-ray diffraction scans. $l_{theoretical}$ is calculated from bulk $BaTiO_3$ lattice parameters[13] (*i.e.*, $a_{bulk} = 3.992$ Å, $c_{bulk} = 4.036$ Å), substrate lattice parameter[47] and a $BaTiO_3$ Poisson's ratio of 0.35[48], under the condition of a biaxial stress state. For a relaxed $BaTiO_3$ film with (001) orientation, $l_{measured}$ is directly obtained from θ-2θ X-ray diffraction scans.

$l_{theoretical}$ takes the value of the *c*-axis lattice parameter in bulk $BaTiO_3$ (*i.e.*, $l_{theoretical} = c_{bulk}$). For a polycrystalline or highly-textured $BaTiO_3$ film with different grain orientations, $l_{measured}$ takes the value of measured pseudocubic cell parameter, $a_{pc,measured}$, calculated from the measured lattice parameters of a tetragonal unit cell[49] (*i.e.*, $l_{measured} = a_{pc,measured} = \sqrt[3]{a_{measured}^2 \times c_{measured}}$), while $l_{theoretical}$ takes the value of theoretical pseudocubic cell parameter, $a_{pc,theoretical}$, calculated from bulk $BaTiO_3$ lattice parameters (*i.e.*, $l_{theoretical} = a_{pc,theoretical} = \sqrt[3]{a_{bulk}^2 \times c_{bulk}} = 4.006$ Å).

Figure 2f. This plot summarizes the energy of switching *vs.* coercive voltage. The energy of switching is calculated from the area enclosed by the saturated polarization-electric field hysteresis loop. Data for $PbZr_xTi_{1-x}O_3$ thin films[50-55] are also shown as comparisons.

II. Coercive Field in $BaTiO_3$ Thin Films Grown on $SrTiO_3$/Si Substrates

Here, we rationalize why the coercive field remains relatively small in $BaTiO_3$ films grown on $SrTiO_3$/Si (001) substrate. The relaxed, bulk-like portions in these $BaTiO_3$ films (specifically the *c* domains, which are the domains oriented in the direction of the device) would, intrinsically, have a lower coercive field[13] (*e.g.*, the coercive field for single crystal $BaTiO_3$ is ~1 kV cm^{-1}) as their strain is relaxed. However, the formation of these relaxed phases are often accompanied by dislocation formation[56], therefore they also contain a certain amount of defects which can increase the coercive field. Moreover, some portion of the films remains strained (thus likely exhibiting a large coercive field[13,57]). This combination, in turn, manifests as having a similar, but slightly larger coercive field (~16.5 kV cm^{-1}) than the coherently strained films (~16.0 kV cm^{-1}) which is still advantageous.

Supplementary Figures

I. Structural Characterization of $BaTiO_3$ Thin Films Grown at Different Pressures

Reciprocal space mapping (RSM) studies of heterostructures of the form 30 nm $SrRuO_3$/100 nm $BaTiO_3$/30 nm $SrRuO_3$/$GdScO_3$ (110) were completed using X-ray diffraction. The $BaTiO_3$ layer was grown at varying pressures (as noted in the main text): 20 mTorr, 40 mTorr, 60 mTorr, and 70 mTorr and RSMs are shown for the heterostructures at each condition (Supplementary Fig. 1a-d). The $BaTiO_3$ films grown at 20 mTorr, 40 mTorr, and 60 mTorr were found to be fully strained on the $SrRuO_3$-buffered $GdScO_3$ substrates while the $BaTiO_3$ heterostructures grown at 70 mTorr are partially relaxed. Increasing the growth pressure from 20 to 60 mTorr leads to a decrease in the out-of-plane lattice parameter (*i.e.*, $\Delta l/l$, or the *c*-axis-lattice expansion, $\Delta c/c$, goes from 1.33% to 0.32% to almost 0% for growth at 20, 40, and 60 mTorr, respectively). X-ray rocking curve studies were done about the 002-diffraction condition for the $BaTiO_3$ and the 220-diffraction condition for the $GdScO_3$ (Supplementary Fig. 1e-h). The full-width-at-half-maximum (FWHM) values of the $BaTiO_3$ films grown at 20 mTorr, 40 mTorr, and 60 mTorr are similar and the FWHM of the 70 mTorr $BaTiO_3$ films is somewhat larger indicating the crystallinity decrease introduced by partial relaxation.

II. Polarization-Electric Field Hysteresis Loops of $BaTiO_3$ Films

Polarization-electric field hysteresis loops were measured on heterostructures of the form 30 nm $SrRuO_3$/100 nm $BaTiO_3$/30 nm $SrRuO_3$/$GdScO_3$ (110) (Supplementary Fig. 2a) and 30 nm $SrRuO_3$/50 nm $BaTiO_3$/30 nm $SrRuO_3$/$GdScO_3$ (110) films (Supplementary Fig. 2b), at a

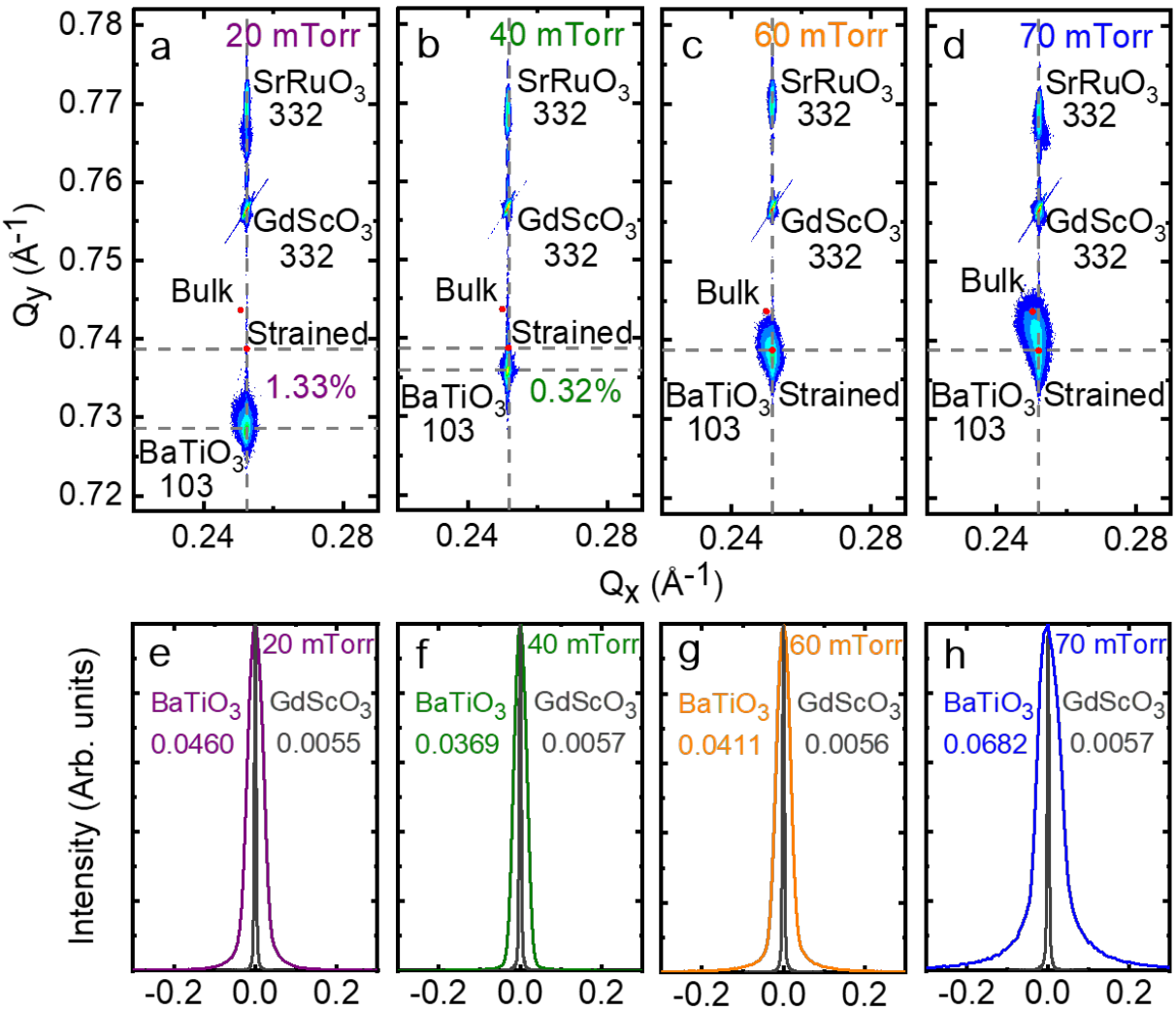

Supplementary Fig. 1. Off-axis reciprocal space mapping studies about the 103- and 332-diffraction conditions of the **a**, 20 mTorr-, **b**, 40 mTorr-, **c**, 60 mTorr-, and **d**, 70 mTorr-grown $BaTiO_3$ films and $SrRuO_3$-buffered-$GdScO_3$ substrate, respectively. Rocking curves about the 002- and 220-diffraction conditions of the **e**, 20 mTorr-, **f**, 40 mTorr-, **g**, 60 mTorr-, and **h**, 70 mTorr-grown $BaTiO_3$ films and $GdScO_3$ substrate, respectively.

frequency of 1 kHz. Again, the $BaTiO_3$ layers were grown at 20 mTorr, 40 mTorr, 60 mTorr, and 70 mTorr. While in all cases robust saturation polarization is observed, the loops for heterostructures grown at 60 mTorr show the best combination of large remanent polarization and small coercive field/voltage. Supplementary Fig. 2c summarizes the coercive field and remanent polarization as a function of growth pressure, indicating the optimal growth pressure of 60 mTorr for the $BaTiO_3$ thin films.

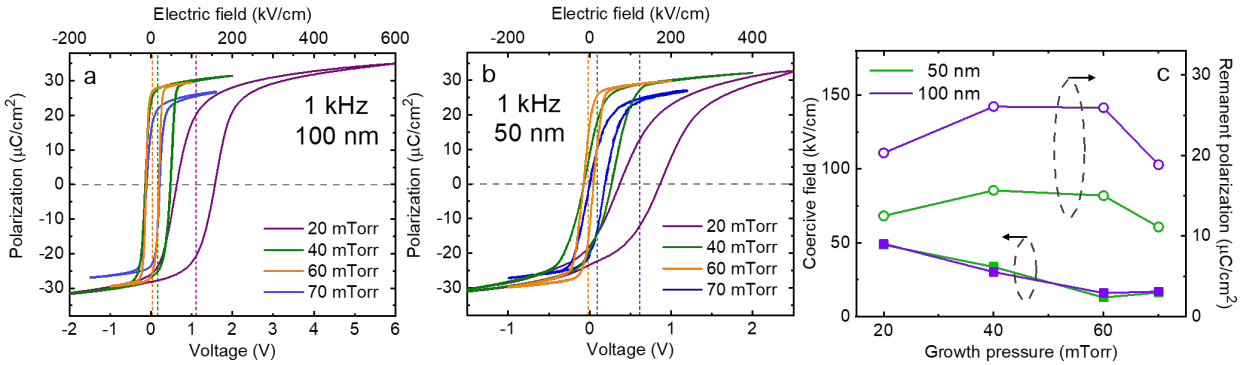

Supplementary Fig. 2. Polarization-electric field hysteresis loops for **a**, 100-nm- and **b**, 50-nm-thick $BaTiO_3$ thin-film heterostructures as a function of growth pressure, measured at a frequency of 1 kHz. **c**, Coercive field (squares, left axis) and remanent polarization (circles, right axis) as a function of growth pressure for 100-nm- and 50-nm-thick $BaTiO_3$ thin film heterostructures.

III. Stoichiometry Characterization

Rutherford backscattering spectrometry (RBS) studies were completed to probe the chemistry of as-grown $BaTiO_3$ heterostructures. A representative set of a data for a 150-nm-thick $BaTiO_3$ thin film grown at 60 mTorr is provided (Supplementary Fig. 3). The orange dotted curve is the experimental data from the Rutherford backscattering spectrum while the black solid curve is the simulation result from the software. The overlap between the orange curve and black curve indicates a good fitting, where the ratio between Ba^{2+} and Ti^{4+} cations is 1:1, indicating near ideal stoichiometry for these films.

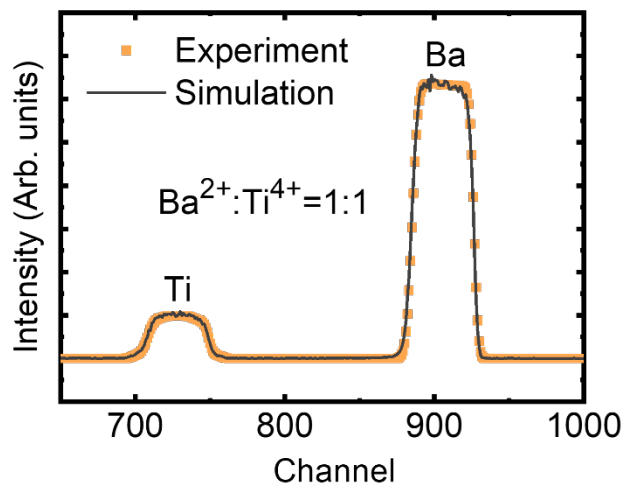

Supplementary Fig. 3. Rutherford backscattering spectrometry of 150 nm $BaTiO_3$ thin film grown at 60 mTorr. The ratio between Ba^{2+} and Ti^{4+} cations is 1:1.

IV. Study of Different Electrode Synthesis and Fabrication Processes

Different top electrode synthesis and fabrication processes were used to produce the 30 nm $SrRuO_3$/100-150 nm $BaTiO_3$/30 nm $SrRuO_3$ capacitor heterostructures, on which frequency-dependent polarization-electric field/voltage hysteresis loops were measured at 1 Hz, 1 kHz, and 10 kHz (Supplementary Fig. 4a-d). With the *ex situ* MgO hard mask process (wherein the top $SrRuO_3$ layer is grown in a separate growth after the $BaTiO_3$ and the bottom $SrRuO_3$ layer), we observe imprint in the hysteresis loops, indicating an asymmetry between the top and bottom $SrRuO_3$-$BaTiO_3$ interfaces. With the *in situ* top $SrRuO_3$ fabrication process (wherein the top and bottom $SrRuO_3$ are grown during the same growth as the $BaTiO_3$), the imprint is much smaller,

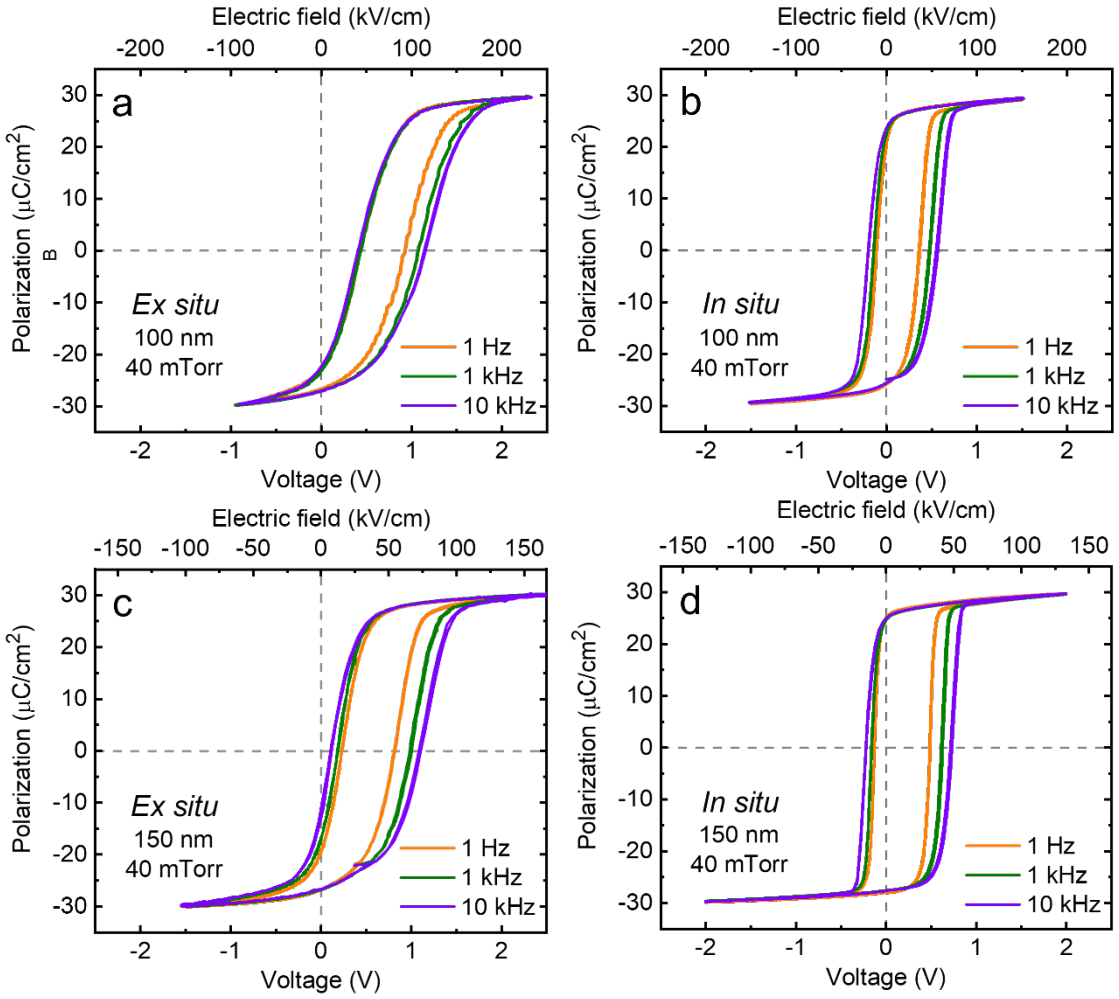

Supplementary Fig. 4. Frequency dependent polarization-voltage/electric field loops of **a,b,** 100-nm- and **c,d,** 150-nm-thick $BaTiO_3$ thin films with top $SrRuO_3$ electrode fabricated with **a,c,** *ex situ* MgO hard mask process and **b,d,** *in situ* growth and etch process.

indicating much more symmetry in top and bottom interfaces. Identification of these tendencies and routes to produce materials with these more idealized interfaces was found to be essential to produce the combination of properties (low coercive field/voltage, robust polarization) desired in this work.

V. Scanning Transmission Electron Microscopy Studies

High angle annular dark field diffraction (HAADF)- Scanning transmission electron microscopy (STEM) studies were completed to probe the structural and interface quality of the $BaTiO_3$ heterostructures (Methods). Representative data is provided for a 30 nm $SrRuO_3$/25 nm $BaTiO_3$/ 30 nm $SrRuO_3$/$GdScO_3$ (110) heterostructure (Supplementary Fig. 5). Low-resolution, wide area scans show films with sharp interfaces, uniform contrast, and no evidence of extended defects, dislocations, etc. (Supplementary Fig. 5a). A zoom-in of the same area reveals the presence of atomically sharp interfaces and nearly ideal epitaxy. Together with the X-ray diffraction data and RBS data, this helps confirm the high-quality nature of the heterostructures and provides a guide for the

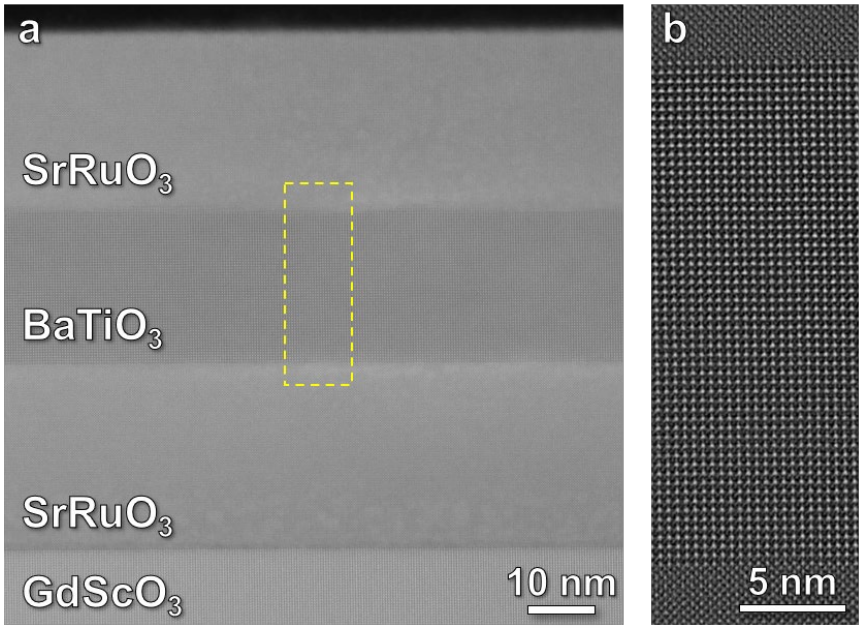

Supplementary Fig. 5. Z-contrast STEM imaging of a 30 nm $SrRuO_3$/25 nm $BaTiO_3$/30 nm $SrRuO_3$/$GdScO_3$ (110) heterostructure showing **a**, materials free of defects, dislocations, etc. across large areas of the film in the low-resolution imaging. **b**, High-resolution image of a typical/representative portion of the films showing pristine interfaces in the heterostructures.

production of the optimized materials – nearly ideal structure, chemistry, interfaces, etc. Such films can likely be accomplished via any growth process, but one must pay close attention to achieving these specific metrics to achieve the desired properties.

VI. Structural Characterization of 125-225 nm $BaTiO_3$ Thin Films

The crystal structure of the 30 nm $SrRuO_3$/125-225 nm $BaTiO_3$/30 nm $SrRuO_3$/$GdScO_3$ (110) heterostructures was characterized using X-ray diffraction (Supplementary Fig. 6). The $BaTiO_3$ films were all grown at the optimized growth condition at 60 mTorr. The resulting θ-2θ scans indicate that all films are epitaxially strained on the $SrRuO_3$-buffered $GdScO_3$ substrate with nearly zero out-of-plane lattice expansion (as small as ~0.16% at film thickness above 200 nm).

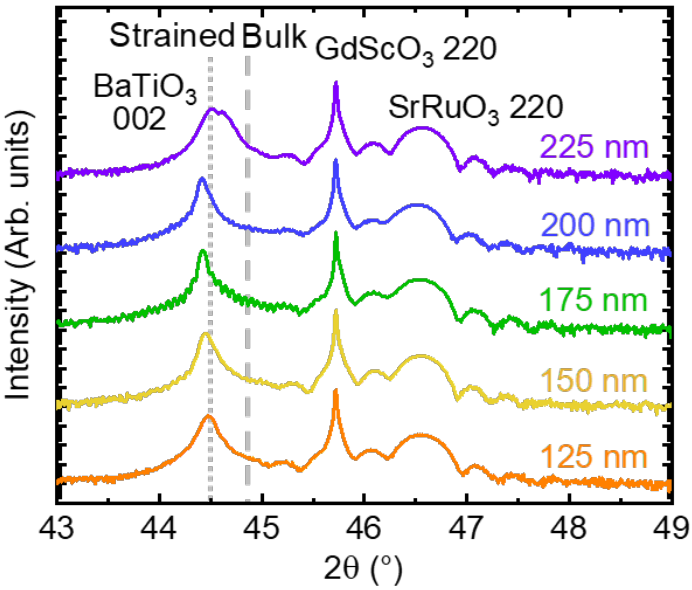

Supplementary Fig. 6. θ-2θ X-ray diffraction scan of 30 nm $SrRuO_3$/125-225 nm $BaTiO_3$/30 nm $SrRuO_3$/$GdScO_3$ (110) heterostructures. The vertical dotted line indicates the theoretical peak position for $BaTiO_3$ film strained on the $GdScO_3$ substrate. The vertical dashed line indicates the peak position for bulk *c*-oriented $BaTiO_3$.

VII. Reciprocal Space Mapping of 12.5-100 nm $BaTiO_3$ Thin Films Grown at 60 mTorr

Reciprocal space mapping (RSM) studies of heterostructures of the form 30 nm $SrRuO_3$/12.5-100 nm $BaTiO_3$/30 nm $SrRuO_3$/$GdScO_3$ (110) were conducted using X-ray diffraction (Supplementary Fig. 7). The $BaTiO_3$ films were all grown at the optimized growth conditions at 60 mTorr. The

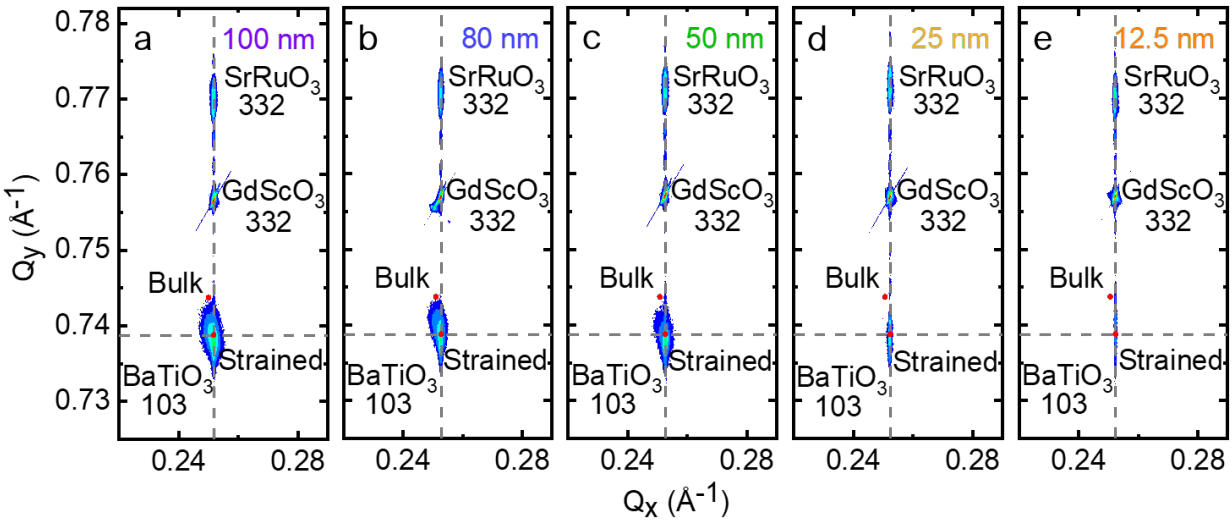

Supplementary Fig. 7. Off-axis reciprocal space mapping studies about the 103- and 332-diffraction conditions of the $BaTiO_3$ films and $SrRuO_3$-buffered-$GdScO_3$ substrate, respectively, for heterostructures with $BaTiO_3$ layer thickness of **a**, 100 nm, **b**, 80 nm, **c**, 50 nm, **d**, 25 nm and **e**, 12.5 nm.

RSM studies indicate all films are epitaxially strained on the $SrRuO_3$-buffered $GdScO_3$ substrates with the $BaTiO_3$ peaks at their theoretical strained positions, with negligible *c*-axis-lattice expansion (<0.02%).

VIII. Polarization-Voltage/Electric Field Hysteresis Loops of $BaTiO_3$ Thin Films

Frequency-dependent polarization-electric field/voltage hysteresis loops were measured on the 30 nm $SrRuO_3$/12.5-225 nm $BaTiO_3$/30 nm $SrRuO_3$/$GdScO_3$ (110) heterostructures in the frequency range from 1 Hz to 10 kHz (Supplementary Fig. 8a-j). The $BaTiO_3$ films were all grown at 60 mTorr.

IX. Piezoresponse Force Microscopy Scans of 25-nm-thick $BaTiO_3$ Thin Films

Piezoresponse force microscopy (PFM) scans were conducted on the 25 nm $BaTiO_3$/30 nm $SrRuO_3$/$GdScO_3$ (110) heterostructures using an atomic force microscope (MFP-3D, Asylum Research). Direct imaging of the as-grown domain state is challenging, likely because of the small

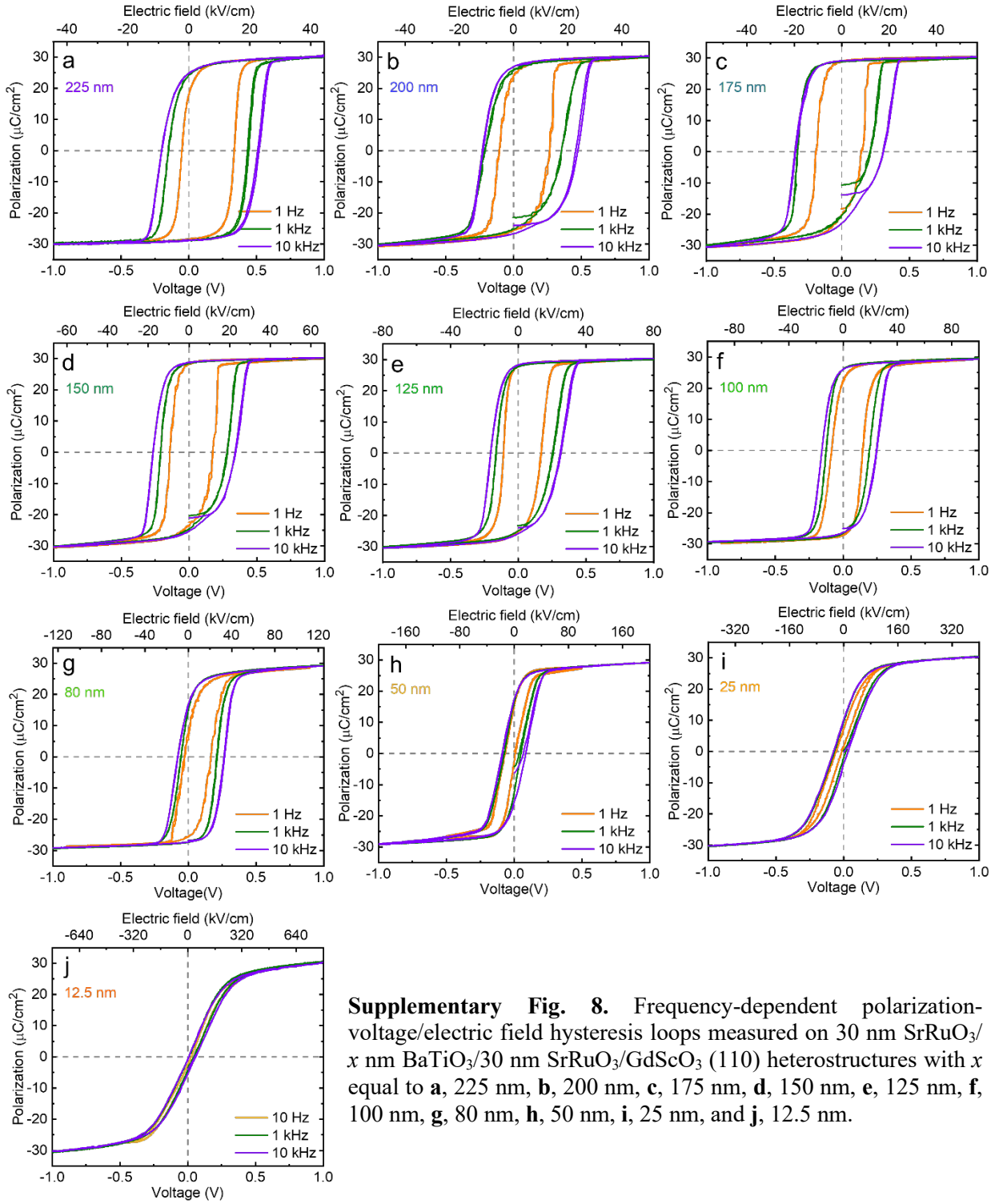

Supplementary Fig. 8. Frequency-dependent polarization-voltage/electric field hysteresis loops measured on 30 nm $SrRuO_3$/ *x* nm $BaTiO_3$/30 nm $SrRuO_3$/$GdScO_3$ (110) heterostructures with *x* equal to **a**, 225 nm, **b**, 200 nm, **c**, 175 nm, **d**, 150 nm, **e**, 125 nm, **f**, 100 nm, **g**, 80 nm, **h**, 50 nm, **i**, 25 nm, and **j**, 12.5 nm.

size of domains and only weak contrast was observed. Furthermore, we poled the film in a box-in-a-box pattern, where the outer box (edge length of 800 nm) was subjected to an applied voltage of -2 V and the inner box (edge length of 400 nm) was subjected to an applied voltage of +2 V

(Supplementary Fig. 9a-d). After poling, we completed the imaging (scanning from the bottom to the top of the image) and each scan took ~5 minutes. Because of the strong depolarization field in the film, and the small size of the domain structures, the phase contrast is still weak, consistent with previous studies reporting unstable polarization in poled ultrathin $BaTiO_3$ films[9]. Moreover, the contrast becomes weaker and weaker even during a single bottom-to-top scan (Supplementary Fig. 9a,c). During the second bottom-to-top scan (finishing after ~10 minutes), the phase and amplitude contrast has almost disappeared (Supplementary Fig. 9b,d), indicating the strong depolarization behavior of the switched area.

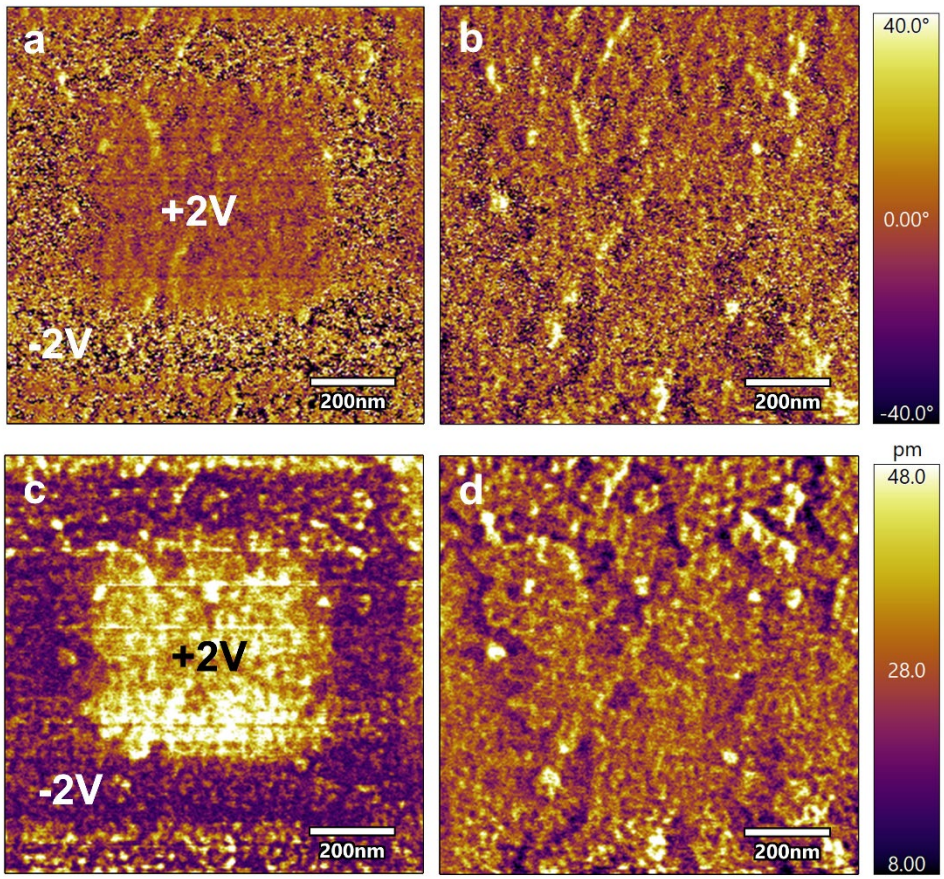

Supplementary Fig. 9. PFM data for poled 25-nm-thick $BaTiO_3$ thin films including phase images after **a**, ~5 minutes and **b**, ~10 minutes and amplitude images after **c**, ~5 minutes and **d**, ~10 minutes after poling a box-in-a-box pattern. The total scan area of all images is 1 μm, and the outer and the inner poled boxes are 800 nm and 400 nm, respectively, across.

X. Fatigue and Retention Measurements

To further probe the performance of the $BaTiO_3$ thin films within ferroelectric-device structures, fatigue measurements were done for heterostructures of the form 30 nm $SrRuO_3$/100 nm $BaTiO_3$/30 nm $SrRuO_3$ /$GdScO_3$ (110) (Supplementary Fig. 10a). The inset shows the Positive-Up-Negative-Down (PUND) pulse sequence applied to the heterostructures to measure the remanent polarization. Each pulse has an amplitude of V_P = 1 V and a width of t_P = 0.15 ms. The delay time between pulses is t_D = 1 ms. The cycling fatigue stress applied is the same as the waveform used in the normal polarization-voltage/electric field hysteresis measurement (bipolar triangle signal with an amplitude of 1 V, at a frequency of 10 kHz). The PUND pulse sequence was applied between cycles. The fatigue measurements showed almost no remanent polarization reduction up to 10^9 cycles when the experiment was terminated.

Retention measurements were also done on the same capacitor structures (Supplementary Fig. 10b). The inset is the modified PUND pulse sequence (representing the first half of the normal PUND measurement) applied to the heterostructure. Each measurement cycle consists of three pulses with same amplitude (V_P = 1 V) and width (t_P = 0.15 ms). The delay time between the first

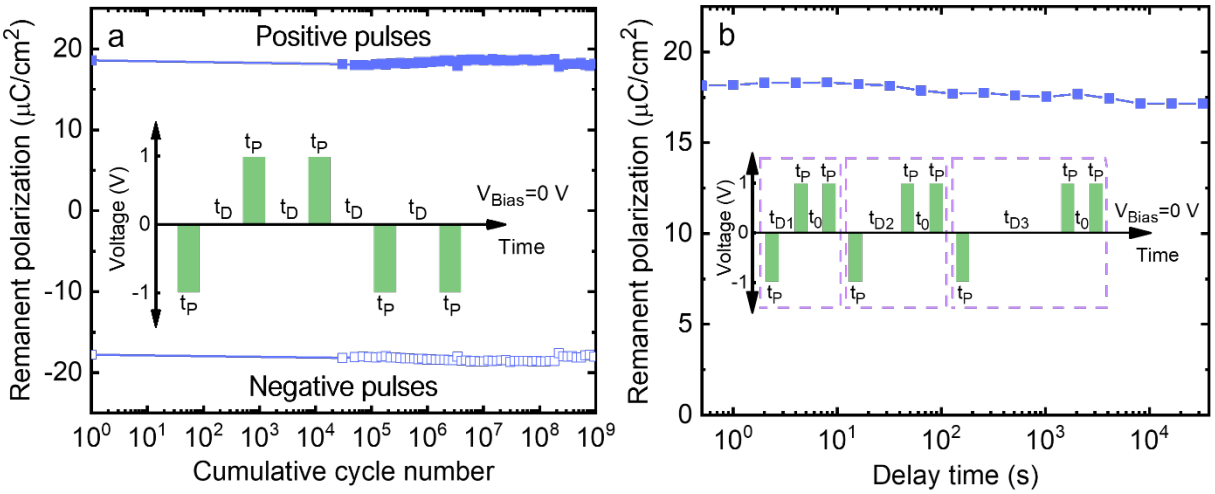

Supplementary Fig. 10. a, Fatigue measurement on 100-nm-thick $BaTiO_3$ films grown at 60 mTorr using cyclic bipolar waveform at a frequency of 10 kHz. Inset: Positive-Up-Negative-Down (PUND) pulse sequence used to measure remanent polarization between fatigue cycles. **b**, Retention measurement on 100-nm-thick $BaTiO_3$ films grown at 60 mTorr. Inset: Modified PUND sequence used to measure the retention behavior of the sample.

pulse and the second pulse, t_{Dn}, is a variable representing the retention time in $BaTiO_3$ films, while the delay time between the second pulse and the third pulse is fixed at t_0 = 1 ms. In each measurement cycle, the total (*i.e.*, switching and non-switching) charge measured from the second pulse is denoted as P_2 while the non-switching charge measured from the third pulse is denoted as P_3. In the initial measurement cycle, t_{Dn} was set at 1 ms (*i.e.*, equivalent to the pulse delay time in fatigue measurement), and the initial remanent polarization was calculated using P_r *(initial)* = (P_2-P_3)/2. In the following measurement cycles, same pulse trains were applied, except that t_{Dn} was set at larger values. For each different t_{Dn} value, the remanent polarization was calculated using $P_r = P_2 - P_3 - P_r$ *(initial)*. The retention measurements showed nearly zero remanent polarization reduction for up to 10 hours when the experiment was terminated. Both fatigue and retention measurements indicate the strong stability of the remanent polarization against cycling stress and retention time.

Same PUND pulse sequences are used for the fatigue and retention measurements on a heterostructure with an imprinted hysteresis loop, except that an additional voltage bias is applied to the heterostructure to compensate the imprint - *e.g.*, for the 30 nm $SrRuO_3$/100 nm $BaTiO_3$/30 nm $SrRuO_3$/20 nm $SrTiO_3$/Si (001) heterostructure, a bias of 0.15 V is applied (insets, Fig. 4c,d).

XI. Switching-Dynamics Measurements on 25 nm $BaTiO_3$ Thin Films

The switching kinetics of 30 nm $SrRuO_3$/25 nm $BaTiO_3$/30 nm $SrRuO_3$ capacitor structures were studied to probe the switching time of the system using pulse measurements. The schematic of the pulse train[58] is shown (Supplementary Fig. 11a). A sequence of three pulses is used to: *1*. Preset the ferroelectric polarization to a well-defined state, *2*. $P_2(t)$ switches the polarization and measures the corresponding total (*i.e.*, switching and non-switching) current and *3*. $P_3(t)$ measures the non-switching dielectric response current through the circuit. By subtracting $P_2 - P_3$, we

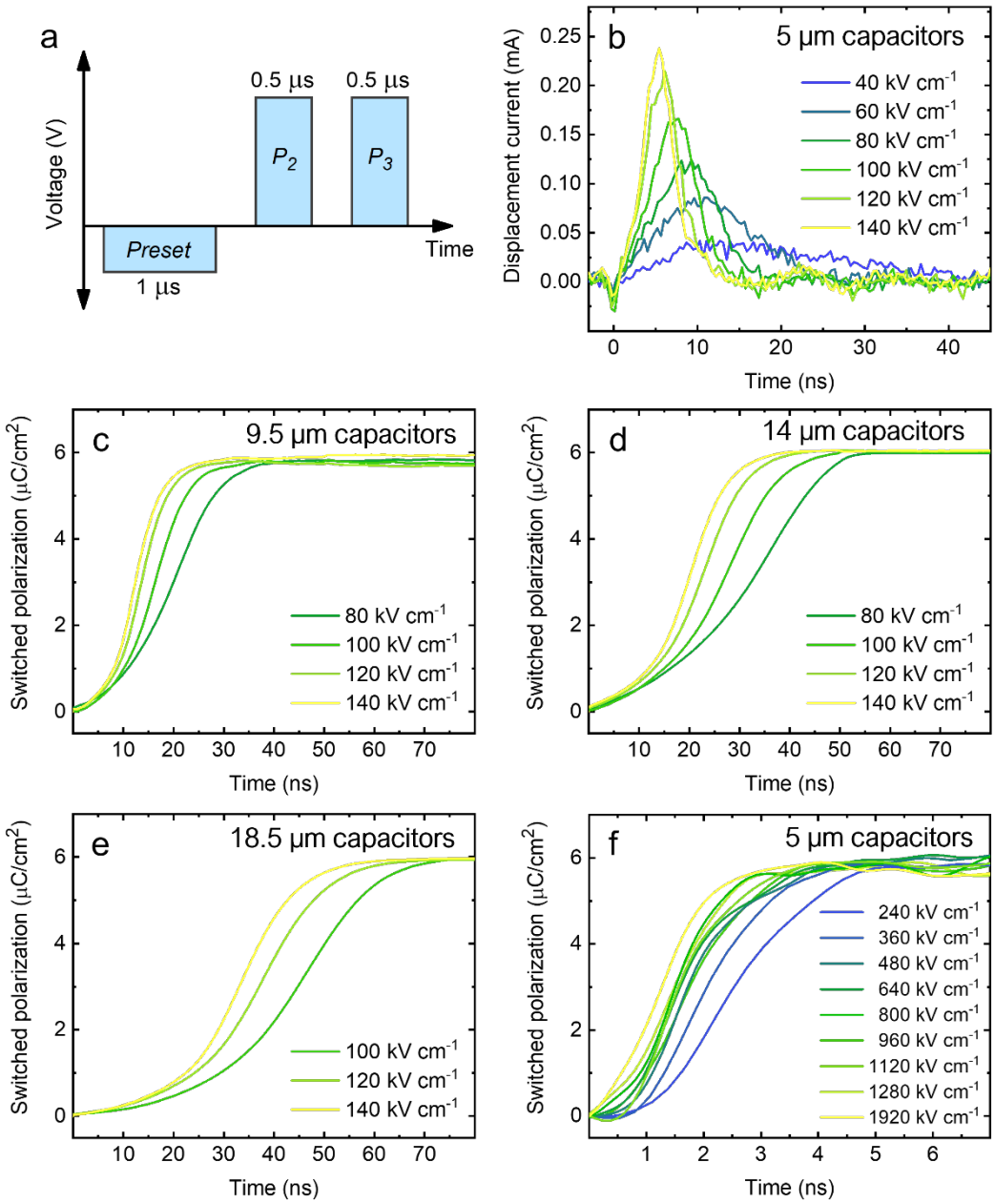

Supplementary Fig. 11. a, Schematic of the pulse train used to study ferroelectric switching dynamics on 30 nm $SrRuO_3$/25 nm $BaTiO_3$/30 nm $SrRuO_3$ capacitor structures. **b,** Time-dependent displacement current of switching at low applied electric fields, measured on 5-µm-diameter capacitors and corresponding to the polarization transient curves in Fig. 3a. Polarization transient curves as a function of applied field, measured on **c**, 9.5-µm-, **d**, 14-µm-, and **e**, 18.5-µm-diameter circular capacitors. **f**, Polarization transient curves at high electric fields, measured on 5-µm-diameter capacitors.

disambiguously extract the displacement current associated with ferroelectric switching alone (Supplementary Fig. 11b). The polarization transient curves are calculated using integration $\Delta P = \int_0^{+\infty}[P_2(t) - P_3(t)]dt$. Shown here is polarization transient data for various capacitor areas and

various applied fields (Supplementary Fig. 11c-f). The characteristic switching time[59], t_{sw}, is extracted from the polarization transient curve, and is defined as $t_{sw} = t$ (90% P_S) – t (10% P_S), where t (10% P_S) and t (90% P_S) are the times needed for the switched polarization to reach 10% and 90% of the its saturation value, respectively. To facilitate comparison amongst polarization transient curves obtained from different applied fields and capacitor sizes, all saturation polarization values are normalized to the value measured on 5-μm-diameter capacitors at 140 kV cm^{-1}.

XII. Lateral Size-Scaling on 50 nm and 100 nm $BaTiO_3$ Thin Films

The characteristic switching time of 30 nm $SrRuO_3$/50-100 nm $BaTiO_3$/30 nm $SrRuO_3$ capacitor structures were studied as a function of capacitor area at an electric field of E = 140 kV cm^{-1} (Supplementary Fig. 12). $BaTiO_3$ heterostructures of all thicknesses (*i.e.*, 25, 50, and 100 nm) follow the same linear scaling law. Moreover, all films with different thicknesses have shown similar switching time at the same electric field, which is expected from the classic Kolmogorov-Avrami-Ishibashi (KAI) model[60] which is regularly used to successfully describe polarization reversal processes in thin-film ferroelectrics[57,61]. In the KAI model,

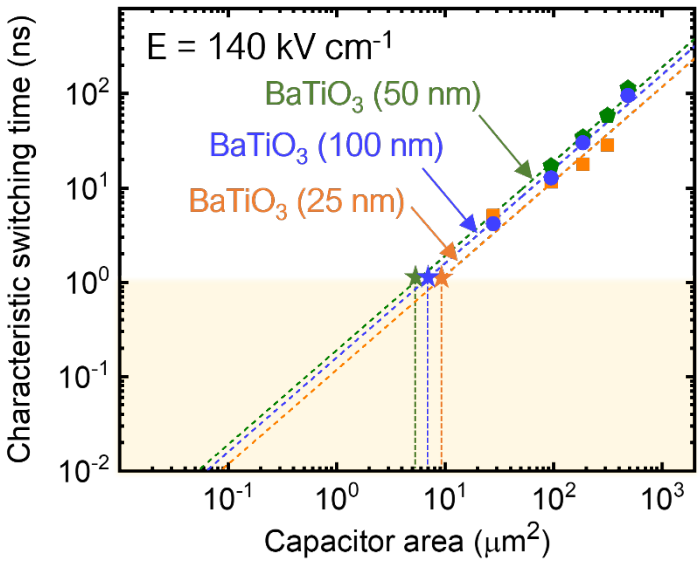

Supplementary Fig. 12. Characteristic switching time as a function of capacitor area on 25-, 50-, and 100-nm-thick $BaTiO_3$ films. The dashed lines are linear fits to the data. The stars are the projected capacitor areas at which sub-ns switching time can be achieved.

the ferroelectric switching process includes domain nucleation, forward domain growth across the thickness of the film, and subsequent sideways growth across the capacitor area. The timescale for forward domain growth in thin films is typically very short (<100 ps), while for sideways domain growth it takes ~ ns or longer depending on various intrinsic and extrinsic factors[62]. Therefore, the time needed for forward domain growth contributes very little to the total switching time and the sideways growth of domain is the rate-limiting step in ferroelectric thin film switching[57]. As a result, the $BaTiO_3$ heterostructures with different thicknesses have shown similar switching times and almost the same projected capacitor area where sub-ns switching can be achieved (green star *vs.* blue star *vs.* orange star, Supplementary Fig. 12).

XIII. Structural Characterization of $BaTiO_3$ Grown on $SrTiO_3$/Si Substrates

The crystal structure of 30 nm $SrRuO_3$/100 nm $BaTiO_3$/30 nm $SrRuO_3$/20 nm $SrTiO_3$/Si (001) heterostructures was characterized using X-ray diffraction (Supplementary Fig. 13). The $BaTiO_3$ films were grown at the optimized conditions at 60 mTorr. Short range θ-2θ X-ray diffraction scan reveals multiple $BaTiO_3$ peaks, including those thought to arise from strained $BaTiO_3$ on $SrTiO_3$/Si substrate (dashed line), that from bulk *c*-oriented $BaTiO_3$ (dash-dotted line), and that from bulk *a*-oriented $BaTiO_3$ (dotted line). The existence of the bulk-like diffraction peaks indicates a partially

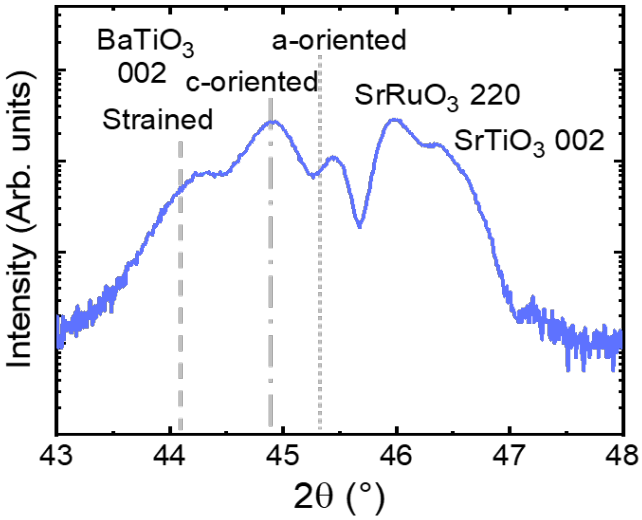

Supplementary Fig. 13. Short range θ-2θ X-ray diffraction scan of the 30 nm $SrRuO_3$/100 nm $BaTiO_3$/30 nm $SrRuO_3$/20 nm $SrTiO_3$/Si (001) heterostructures.

relaxed $BaTiO_3$ film due to large thermal stresses induced by the underlying silicon[27] and large lattice mismatch between bulk $BaTiO_3$ and the $SrTiO_3$ buffer layer (~2.4%)[13,63].

XIV. Dielectric Constant-Voltage Measurements

Dielectric constant-voltage measurements were done on the 30 nm $SrRuO_3$/12.5-100 nm $BaTiO_3$/30 nm $SrRuO_3$/$GdScO_3$ (110) heterostructures at a frequency of 10 kHz (Supplementary Fig. 14). The $BaTiO_3$ films were grown at 60 mTorr.

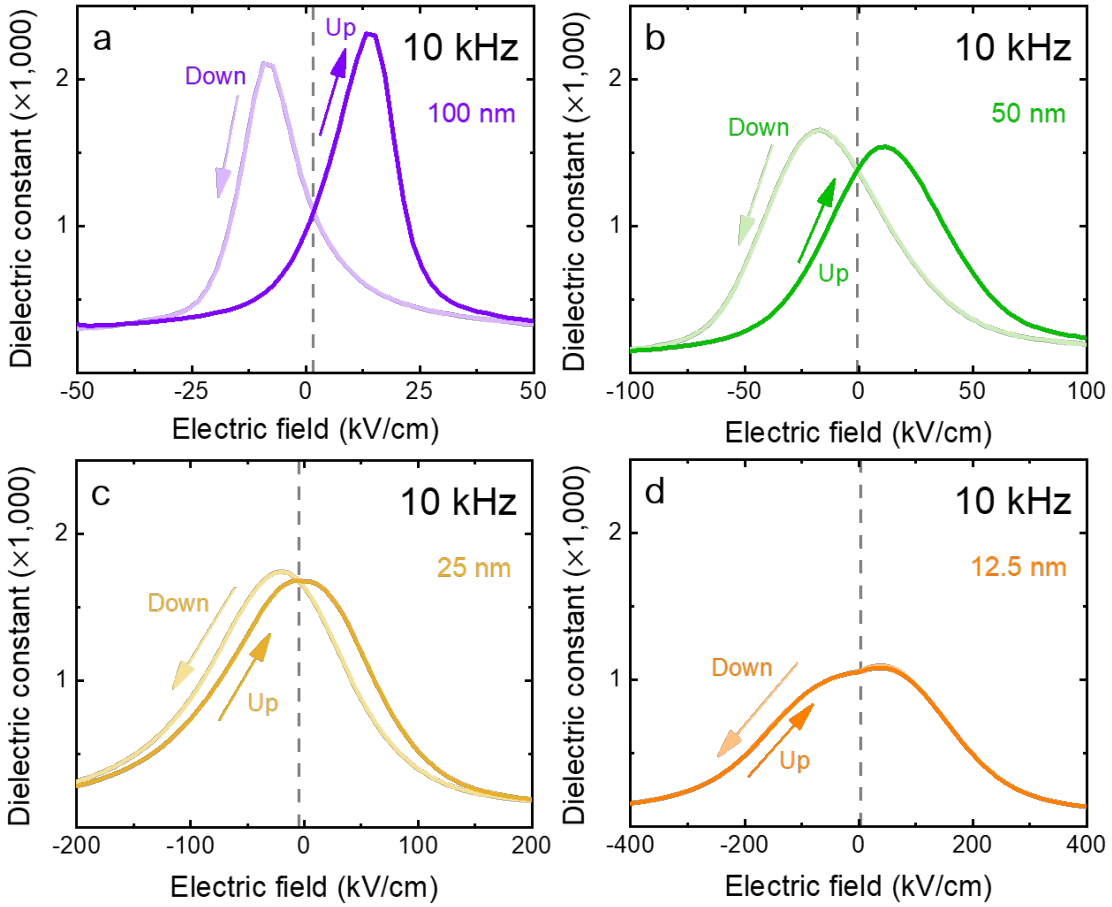

Supplementary Fig. 14. Dielectric constant-voltage measurements on **a**, 100-nm-, **b**, 50-nm-, **c**, 25-nm-, and **d**, 12.5-nm-thick $BaTiO_3$ thin films.

Supplementary References

1. Nagatomo, T., Kosaka, T., Omori, S. & Omoto, O. Fabrication of $BaTiO_3$ films by RF planar-magnetron sputtering. *Ferroelectrics* **37**, 681-684 (1981).
2. Abe, K., Komatsu, S., Yanase, N., Sano, K. & Kawakubo, T. Asymmetric ferroelectricity and anomalous current conduction in heteroepitaxial $BaTiO_3$ thin films. *Jpn. J. Appl. Phys.* **36**, 5846-5853 (1997).
3. Yanase, N., Abe, K., Fukushima, N. & Kawakubo, T. Thickness dependence of ferroelectricity in heteroepitaxial $BaTiO_3$ thin film capacitors. *Jpn. J. Appl. Phys.* **38**, 5305-5308 (1999).
4. Yasumoto, T., Yanase, N., Abe, K. & Kawakubo, T. Epitaxial growth of $BaTiO_3$ thin films by high gas pressure sputtering. *Jpn. J. Appl. Phys.* **39**, 5369-5373 (2000).
5. Qiao, L. & Bi, X. Microstructure and ferroelectric properties of $BaTiO_3$ films on $LaNiO_3$ buffer layers by rf sputtering. *J. Cryst. Growth* **310**, 2780-2784 (2008).
6. Qiao, L. & Bi, X. Origin of compressive strain and phase transition characteristics of thin $BaTiO_3$ film grown on $LaNiO_3$/Si substrate. *Phys. Status Solidi A* **207**, 2511-2516 (2010).
7. Zhang, W. *et al.* Space-charge dominated epitaxial $BaTiO_3$ heterostructures. *Acta Mater.* **85**, 207-215 (2015).
8. Wague, B., Baboux, N., Romeo, P. R., Robach, Y. & Vilquin, B. Comparison of epitaxial and textured ferroelectric $BaTiO_3$ thin films. *J. Mod. Phys.* **11**, 509-516 (2020).
9. Dubourdieu, C. *et al.* Switching of ferroelectric polarization in epitaxial $BaTiO_3$ films on silicon without a conducting bottom electrode. *Nat. Nanotechnol.* **8**, 748-754 (2013).
10. Mazet, L., Yang, S. M., Kalinin, S. V., Schamm-Chardon, S. & Dubourdieu, C. A review of molecular beam epitaxy of ferroelectric $BaTiO_3$ films on Si, Ge and GaAs substrates and their applications. *Sci. Technol. Adv. Mater.* **16**, 036005 (2015).
11. Morgan, T. A. *et al.* Self-assembled stoichiometric barium titanate thin films grown by molecular beam epitaxy. *J. Cryst. Growth* **493**, 15-19 (2018).
12. Abel, S. *et al.* Large Pockels effect in micro-and nanostructured barium titanate integrated on silicon. *Nat. Mater.* **18**, 42-47 (2019).
13. Choi, K. J. *et al.* Enhancement of ferroelectricity in strained $BaTiO_3$ thin films. *Science* **306**, 1005-1009 (2004).
14. Cheng, H.-F., Yeh, M.-H., Liu, K.-S. & Lin, I.-N. Characteristics of $BaTiO_3$ films prepared by pulsed laser deposition. *Jpn. J. Appl. Phys.* **32**, 5656-5660 (1993).
15. Nashimoto, K., Fork, D. K., Ponce, F. A. & Tramontana, J. C. Epitaxial $BaTiO_3$/MgO structure grown on GaAs (100) by pulsed laser deposition. *Jpn. J. Appl. Phys.* **32**, 4099-4102 (1993).
16. Watanabe, Y., Matsumoto, Y., Kunitomo, H., Tanamura, M. & Nishimoto, E. Crystallographic and electrical properties of epitaxial $BaTiO_3$ film grown on conductive and insulating perovskite oxides. *Jpn. J. Appl. Phys.* **33**, 5182-5186 (1994).
17. Srikant, V., Tarsa, E., Clarke, D. & Speck, J. Crystallographic orientation of epitaxial $BaTiO_3$ films: The role of thermal-expansion mismatch with the substrate. *J. Appl. Phys.* **77**, 1517-1522 (1995).
18. Lin, W. *et al.* Growth and ferroelectricity of epitaxial-like $BaTiO_3$ films on single-crystal MgO, $SrTiO_3$, and silicon substrates synthesized by pulsed laser deposition. *J. Appl. Phys.* **77**, 6466-6471 (1995).
19. Kullmer, R. Dielectric and ferroelectric properties of pulsed-laser deposited $BaTiO_3$ films. *Appl. Phys. A* **65**, 273-279 (1997).

20. Li, C., Chen, Z., Zhou, Y. & Cui, D. Effect of oxygen content on the dielectric and ferroelectric properties of laser-deposited $BaTiO_3$ thin films. *J. Phys. Condens. Matter* **13**, 5261-5268 (2001).
21. Drezner, Y. & Berger, S. Nanoferroelectric domains in ultrathin $BaTiO_3$ films. *J. Appl. Phys.* **94**, 6774-6778 (2003).
22. Kim, D. *et al.* Polarization relaxation induced by a depolarization field in ultrathin ferroelectric $BaTiO_3$ capacitors. *Phys. Rev. Lett.* **95**, 237602 (2005).
23. Jo, J., Kim, Y., Noh, T., Yoon, J.-G. & Song, T. Coercive fields in ultrathin $BaTiO_3$ capacitors. *Appl. Phys. Lett.* **89**, 232909 (2006).
24. Kan, D. & Shimakawa, Y. Controlled cation stoichiometry in pulsed laser deposition-grown $BaTiO_3$ epitaxial thin films with laser fluence. *Appl. Phys. Lett.* **99**, 081907 (2011).
25. Radaelli, G., Brivio, S., Fina, I. & Bertacco, R. Correlation between growth dynamics and dielectric properties of epitaxial $BaTiO_3$ films. *Appl. Phys. Lett.* **100**, 102904 (2012).
26. Dix, N. *et al.* Large out-of-plane ferroelectric polarization in flat epitaxial $BaTiO_3$ on $CoFe_2O_4$ heterostructures. *Appl. Phys. Lett.* **102**, 172907 (2013).
27. Scigaj, M. *et al.* Ultra-flat $BaTiO_3$ epitaxial films on Si (001) with large out-of-plane polarization. *Appl. Phys. Lett.* **102**, 112905 (2013).
28. Damodaran, A. R., Breckenfeld, E., Chen, Z., Lee, S. & Martin, L. W. Enhancement of ferroelectric Curie temperature in $BaTiO_3$ films via strain-induced defect dipole alignment. *Adv. Mater.* **26**, 6341-6347 (2014).
29. Park, D. *et al.* Studies of local structural distortions in strained ultrathin $BaTiO_3$ films using scanning transmission electron microscopy. *Microsc. Microanal.* **20**, 740-747 (2014).
30. Liu, F. *et al.* Selecting steady and transient photocurrent response in $BaTiO_3$ films. *Adv. Electron. Mater.* **1**, 1500171 (2015).
31. Li, M. *et al.* Controlling resistance switching polarities of epitaxial $BaTiO_3$ films by mediation of ferroelectricity and oxygen vacancies. *Adv. Electron. Mater.* **1**, 1500069 (2015).
32. Scigaj, M. *et al.* High ferroelectric polarization in c-oriented $BaTiO_3$ epitaxial thin films on $SrTiO_3$/Si (001). *Appl. Phys. Lett.* **109**, 122903 (2016).
33. Bhatia, B. *et al.* High power density pyroelectric energy conversion in nanometer-thick $BaTiO_3$ films. *Nanoscale Microscale Thermophys. Eng.* **20**, 137-146 (2016).
34. Yamada, H., Toyosaki, Y. & Sawa, A. Coherent epitaxy of a ferroelectric heterostructure on a trilayered buffer for integration into silicon. *Adv. Electron. Mater.* **2**, 1500334 (2016).
35. Negulescu, B. *et al.* Nonlinear piezoelectric properties of epitaxial $BaTiO_3$ thin film. *Ferroelectrics* **514**, 9-18 (2017).
36. Dasgupta, A. *et al.* Nonstoichiometry, structure, and properties of $Ba_{1-x}TiO_y$ thin films. *J. Mater. Chem. C* **6**, 10751-10759 (2018).
37. Lyu, J. *et al.* Control of polar orientation and lattice strain in epitaxial $BaTiO_3$ films on silicon. *ACS Appl. Mater. Interfaces* **10**, 25529-25535 (2018).
38. Lyu, J., Fina, I., Solanas, R., Fontcuberta, J. & Sánchez, F. Tailoring lattice strain and ferroelectric polarization of epitaxial $BaTiO_3$ thin films on Si (001). *Sci. Rep.* **8**, 495 (2018).
39. Kobayashi, S., Inoue, K., Kato, T., Ikuhara, Y. & Yamamoto, T. Multiphase nanodomains in a strained $BaTiO_3$ film on a $GdScO_3$ substrate. *J. Appl. Phys.* **123**, 064102 (2018).
40. Peng, W. *et al.* Constructing polymorphic nanodomains in $BaTiO_3$ films via epitaxial symmetry engineering. *Adv. Funct. Mater.* **30**, 1910569 (2020).

41. Iijima, K., Terashima, T., Yamamoto, K., Hirata, K. & Bando, Y. Preparation of ferroelectric $BaTiO_3$ thin films by activated reactive evaporation. *Appl. Phys. Lett.* **56**, 527-529 (1990).
42. Terauchi, H. *et al.* Structural study of epitaxial $BaTiO_3$ crystals. *J. Phys. Soc. Jpn.* **61**, 2194-2197 (1992).
43. Yoneda, Y. *et al.* Ferroelectric phase transition in $BaTiO_3$ films. *J. Phys. Soc. Jpn.* **62**, 1840-1843 (1993).
44. Li, A. *et al.* Fabrication and electrical properties of sol-gel derived $BaTiO_3$ films with metallic $LaNiO_3$ electrode. *Appl. Phys. Lett.* **70**, 1616-1618 (1997).
45. Zhou, Z., Lin, Y., Tang, H. & Sodano, H. A. Hydrothermal growth of highly textured $BaTiO_3$ films composed of nanowires. *Nanotechnol.* **24**, 095602 (2013).
46. Lee, E. *et al.* Preparation and properties of ferroelectric $BaTiO_3$ thin films produced by the polymeric precursor method. *J. Mater. Sci. Lett.* **19**, 1457-1459 (2000).
47. Damodaran, A. R. *et al.* New modalities of strain-control of ferroelectric thin films. *J. Phys. Condens. Matter* **28**, 263001 (2016).
48. Dent, A., Bowen, C., Stevens, R., Cain, M. & Stewart, M. Effective elastic properties for unpoled barium titanate. *J. Eur. Ceram. Soc.* **27**, 3739-3743 (2007).
49. Smith, M. B. *et al.* Crystal structure and the paraelectric-to-ferroelectric phase transition of nanoscale $BaTiO_3$. *JACS* **130**, 6955-6963 (2008).
50. Lee, J. & Desu, S. The shifting of PE hysteresis loop by the asymmetric contacts on ferroelectric PZT thin films. *Ferroelectr. Lett. Sect.* **20**, 27-34 (1995).
51. Izyumskaya, N. *et al.* Structural and electrical properties of $Pb(Zr, Ti)O_3$ films grown by molecular beam epitaxy. *Appl. Phys. Lett.* **91**, 182906 (2007).
52. Nguyen, M. D. *et al.* Research update: enhanced energy storage density and energy efficiency of epitaxial $Pb_{0.9}La_{0.1}(Zr_{0.52}Ti_{0.48})O_3$ relaxor-ferroelectric thin-films deposited on silicon by pulsed laser deposition. *APL Mater.* **4**, 080701 (2016).
53. Xu, R. *et al.* Reducing coercive-field scaling in ferroelectric thin films via orientation control. *ACS Nano* **12**, 4736-4743 (2018).
54. Saremi, S. *et al.* Local control of defects and switching properties in ferroelectric thin films. *Phys. Rev. Mater.* **2**, 084414 (2018).
55. Shin, C. Experimental understanding of polarization switching in PZT ferroelectric capacitor. *Semicond. Sci. Technol.* **34**, 075004 (2019).
56. Catalan, G., Noheda, B., McAneney, J., Sinnamon, L. & Gregg, J. Strain gradients in epitaxial ferroelectrics. *Phys. Rev. B* **72**, 020102 (2005).
57. Pesquera, D. *et al.* Beyond substrates: strain engineering of ferroelectric membranes. *Adv. Mater.* **32**, 2003780 (2020).
58. Parsonnet, E. *et al.* Toward intrinsic ferroelectric switching in multiferroic $BiFeO_3$. *Phys. Rev. Lett.* **125**, 067601 (2020).
59. Li, J. *et al.* Ultrafast polarization switching in thin-film ferroelectrics. *Appl. Phys. Lett.* **84**, 1174-1176 (2004).
60. Ishibashi, Y. & Takagi, Y. Note on ferroelectric domain switching. *J. Phys. Soc. Jpn.* **31**, 506-510 (1971).
61. Saremi, S. *et al.* Electronic transport and ferroelectric switching in ion-bombarded, defect-engineered $BiFeO_3$ thin films. *Adv. Mater. Interfaces* **5**, 1700991 (2018).
62. Hu, W. J. *et al.* Universal ferroelectric switching dynamics of vinylidene fluoride-trifluoroethylene copolymer films. *Sci. Rep.* **4**, 4772 (2014).

63. Zhang, L. *et al.* Continuously tuning epitaxial strains by thermal mismatch. *ACS nano* **12**, 1306-1312 (2018).